Effect of Graphene Oxide on the Properties of Its Composite with Polyaniline

Hualan Wang, Qingli Hao,* Xujie Yang, Lude Lu, and Xin Wang*

Key Laboratory of Soft Chemistry and Functional Materials, Ministry of Education, Nanjing University of Science and Technology, Nanjing, P.R. China

ABSTRACT Graphene oxide, a single layer of graphite oxide (GO), has been used to prepare graphene oxide/polyaniline (PANI) composite with improved electrochemical performance as supercapacitor electrode by in situ polymerization using a mild oxidant. The composites are synthesized under different mass ratios, using graphite as start material with two sizes: 12 500 and 500 mesh. The result shows that the morphology of the prepared composites is influenced dramatically by the different mass ratios. The composites are proposed to be combined through electrostatic interaction (doping process), hydrogen bonding, and $\pi-\pi$ stacking interaction. The highest initial specific capacitances of 746 F g^{-1} (12 500 mesh) and 627 F g^{-1} (500 mesh) corresponding to the mass ratios 1:200 and 1:50 (graphene oxide/aniline) are obtained, compared to PANI of 216 F g^{-1} at 200 mA g^{-1} by charge−discharge analysis between 0.0 and 0.4 V. The improved capacitance retention of 73% (12 500 mesh) and 64% (500 mesh) after 500 cycles is obtained for the mass ratios 1:23 and 1:19 compared to PANI of 20%. The enhanced specific capacitance and cycling life implies a synergistic effect between two components. This study is of significance for developing new doped PANI materials for supercapacitors.

KEYWORDS: graphene • graphene oxide • polyaniline • electrochemical properties • supercapacitor

INTRODUCTION

Supercapacitors are the promising power source and have attracted considerable attention in recent years (1−3). The increasing pollution due to electrical vehicles and explosive growth of portable electronic devices has pushed the development of high-performance supercapacitors as the urgent requirement. There are two main classes of electrochemical capacitors based upon charge-storage mechanism: (a) electrical double-layer capacitors (EDLCs) in which the capacitance arises from the charge separation at the electrode/electrolyte interface and (b) redox supercapacitors in which the pseudocapacitance arises from faradic reactions occurring at the electrode/electrolyte interface (4). High-surface carbons, noble metal oxides, and conducting polymers are the main families of electrode materials being studied for supercapacitor applications. Conductive polymers have been extensively studied in supercapacitors. The main conductive polymer materials that have been investigated for the supercapacitor electrode are polyaniline (PANI) (5), polypyrrole (PPY) (6), polythiophene (PTH) and their derivatives (7), and so on. Among these polymers, PANI is considered the most promising material because of its high capacitive characteristics, low cost, and ease of synthesis (8, 9). However, the relative poor cycling life restricts its practical applications. Recently, advancement of nanoscale binding technique provides an innovative route to prepare PANI-based composites with better performance as electrode material (10−12). It has been demonstrated that PANI composite with metal oxides exhibit improved supercapacitor performance (13).

Graphene is a two-dimensional form of graphite, the high surface area, excellent mechanical properties and conductivity (14, 15) of this new material have attracted great interests (16−22). Graphene oxide, bearing oxygen functional groups on their basal planes and edges, is a single sheet of graphite oxide and exhibits good performance. It can be obtained by exfoliation of graphite oxide (23). The tunable oxygenous functional groups of graphene oxide facilitate the modification on the surface (24) and make it a promising material for composites with other materials. Recent reports on ultracapacitors based on graphene (14, 25) have attracted great interest. Many graphene composites with conducting polymers have been developed (26, 27). However, the effect of raw graphite material sizes and feeding ratios on the electrochemical properties of such composites have not been investigated intensively.

In our previous work (28), a simple in situ polymerization method was reported to synthesize the nanocomposites of graphene-oxide-doped PANI (GP) which were used as electrode materials. Herein, serious GP composites with different feeding ratios from raw graphite of two sizes have been prepared through in situ polymerization by using a mild oxidant. The introduction of less amount of graphene oxide into PANI is found to greatly enhance the electrochemical performance of PANI. The influence of raw material sizes and feeding ratios on the electrochemical capacitance and chemical structures of GP composites have been investigated systematically.

EXPERIMENTAL SECTION

Materials Synthesis. Graphite oxide was synthesized from powdered flake graphite (12500, 500 mesh) by a modified

* To whom correspondence should be addressed. Tel/Fax: +86 25 84315054. E-mail: haoqingli@yahoo.com (Q.H.); wangx@mail.njust.edu.cn (X.W.).
Received for review November 23, 2009 and accepted February 22, 2010

DOI: 10.1021/am900815k

Hummers method (29). Nanocomposites with different mass ratios (from 1:370 to 1:10) and raw material sizes were synthesized. The typical route, for example, when the mass ratio of graphite oxide/aniline is 1:50, is as follows. Before polymerization, aniline (3.7 mL) was added into an aqueous solution of graphite oxide with a mass ratio of 1:50 under ultrasonication (220 V, 250 W); after being ultrasonicated for 1 h, the graphite oxide was exfoliated to graphene oxide and a stable mixture of aniline/graphene oxide was obtained (28, 30). The chemical polymerization was then performed by the slow addition of H_2O_2 (4.1 mL, 30%), hydrochloric acid (3.3 mL, 37%), and 0.1 mol L^{-1} $FeCl_3 \cdot 6H_2O$ (0.8 mL) under violent stirring to form a 200 mL solution (31). The suspension was kept in an ice bath and stirred for 24 h. The products were then filtered and washed with a large amount of 0.1 mol L^{-1} HCl and acetone and dried at 60 °C for 24 h under a vacuum. The nanocomposites synthesized from different graphite sizes and ratios are signed as S-GP_{ratio} for 12 500 mesh graphite and B-GP_{ratio} for 500 mesh graphite, respectively, like S-$GP_{1:50}$, indicating that the mass ratio of graphene oxide (12500 mesh) and aniline is 1:50. Herein, the pure PANI was synthesized chemically in the absence of graphite oxide via the similar procedure above.

General Characterization. The chemical character and morphology of the samples were analyzed by X-ray photoelectron spectroscopy (XPS, Thermo ESCALAB 250), Raman (RENISHAW inVia Raman Microscope), scanning electron microscopy (SEM, JEOL JSM-6380LV), and transmission electron microscopy (JEM-2100), respectively.

Electrochemical Characterization. The test electrodes were prepared by mixing the sample, acetylene black, and polytetrafluoroethylene in the mass ratio 85:10:5, the mixture was dissolved in distilled water and grinded adequately to form a slurry. The slurry was coated onto a stainless steel, pressed at 10 MPa, and dried under vacuum at 60 °C for 24 h. All electrochemical experiments were carried out in 1 M H_2SO_4 using a three-electrode system, in which platinum foils and saturated calomel electrode (SCE) were used as counter and reference electrodes. Cyclic voltammetry (CV) and electrochemical impedance spectroscopy (EIS) measurements were performed with a CHI660B workstation. The scan rate of CV was in the range from 1 mV s^{-1} to 100 mV s^{-1}. EIS was recorded under the condition: AC voltage amplitude 5 mV, frequency range 1×10^5 to 1×10^{-3} Hz at 0.5 V. Galvanostatic charge−discharge testing was done from 0 to 0.8 V, using a Land Battery workstation at 22 °C.

RESULTS AND DISCUSSION

Morphology Characterizations. The typical microstructures of S-GPratio, PANI and graphene oxide synthesized from graphite with the size 12500 mesh, are presented in Figure 1. The exfoliated layered structure for graphene oxide agglomerate (Figure 1a) can be observed, which is consistent with the report given by Dikin et al. (23). The pure PANI shows short fibrillar and granular agglomerate (Figure 1b). The composite morphology differs from individual components and changes with the increased feeding ratio of two raw materials. The composite S-$GP_{1:100}$ show fibrillar morphology with dimensions of about 300 nm in diameter and 2−3 μm in length, and the large fibers are in fact built from smaller nanofibers about 30 nm in diameter and 100−150 nm in length on the surface, and nanosheets in the backbone of the fibers, as shown in Figure 1c,e. However, with the increase in graphene oxide ratio, the composite S-$GP_{1:23}$ exhibits mainly unregular morphology with multishapes including both fibrillar and agglomeration (Figure 1d,f). The tremendous changes in morphology reveal that the introduction of graphene oxide and the feeding ratio play an important role in adjusting the surface shape in the synthesis process, which may affect the electrochemical performances greatly.

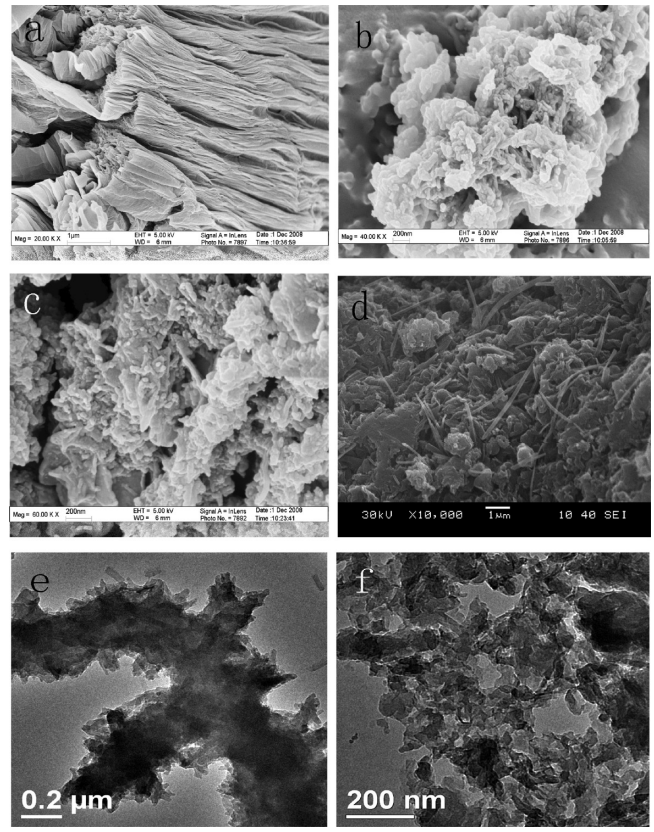

FIGURE 1. SEM images of (a) graphene oxide agglomerate particles, (b) PANI, (c) S-$GP_{1:100}$, and (d) S-$GP_{1:23}$ and TEM images of (e) S-$GP_{1:100}$ and (f) S-$GP_{1:23}$.

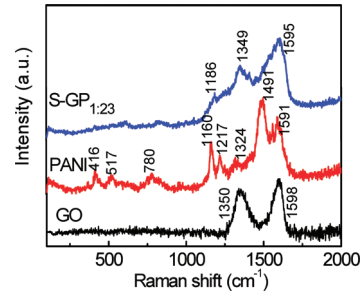

FIGURE 2. Raman spectra of S-GP_{ratio}, graphite oxide, and PANI (λ = 514 nm).

Chemical Analysis. Figure 2 demonstrates the Raman spectra of graphite oxide, PANI and S-$GP_{1:23}$. The Raman spectrum of as-prepared graphite oxide displays two prominent peaks at 1350 and 1598 cm^{-1} that correspond to the D and G modes, respectively (15, 32). The G mode is related to the vibration of sp^2-hybridized carbon. The phonon mode at 1350 cm^{-1}, also known as the D mode, corresponds to the conversion of a sp^2-hybridized carbon to a sp^3-hybridized carbon (33). For pure PANI, out-of-plane C−H wag, out-of-plane C−N−C torsion, imine deformation, in-plane C−H bending, in-plane ring deformation, C−$N^{\bullet+}$ stretching, C═N stretching of quinoid, C−C stretching of benzoid situated at

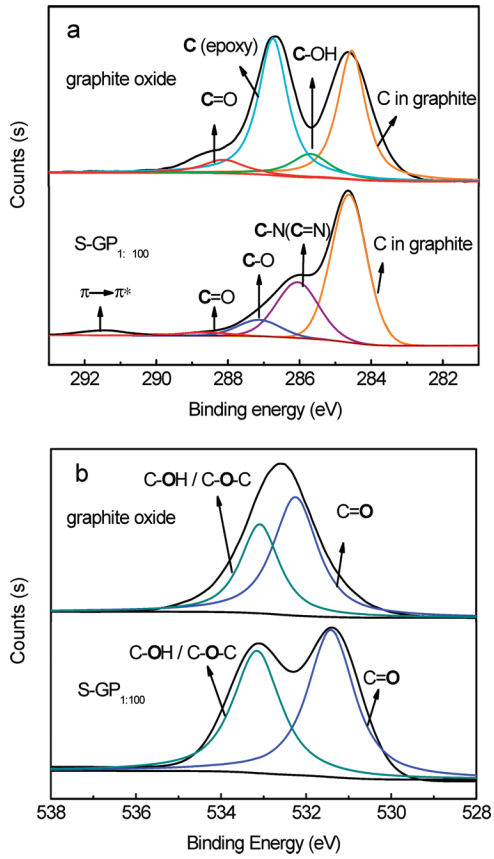

FIGURE 3. XPS spectra in the (a) C 1s and (b) O 1s region of: top, graphite oxide; bottom, S-GP$_{1:100}$.

416, 517, 780, 1160, 1217, 1324, 1491, and 1591 cm^{-1} were observed (34−36). The peaks at 1160, 1324, and 1591 cm^{-1} indicate the doped PANI structure and shift to 1186, 1349, and 1595 cm^{-1} when graphite oxide was introduced into the synthesis process of PANI in the form of graphene oxide. This is probably due to the doping of carboxyl acid of graphene oxide to PANI backbone and $\pi-\pi$ stacking of PANI and graphene oxides sheets. The result reveals that PANI was also in a doped state in the composite, and this observation was also supported by the XPS analysis and UV−vis absorption spectra presented below.

The C 1s and O 1s core-level spectra of graphite oxide and that of S-GP$_{1:100}$ are depicted in panels a and b in Figure 3, respectively. For graphite oxide, the XPS peaks of C 1s in Figure 3a are reasonably decomposed into four Gaussian peaks with binding energies of 288.0 (C═O), 286.7 (C−O−C), 285.7 (C−OH), and 284.6 eV (C−C/C-H) (37), respectively. When combined with PANI in GP$_{1:100}$, the peaks corresponding to C−O−C and C−OH of graphite oxide disappeared and formed a new peak situated at 287.2 eV. This is probably due to the increased conjugation and the hydrogen bonds between the PANI backbone and graphene oxide sheets. These interactions lead to the shift in the C−O−C and C−OH binding energy and consequently the merging of the two peaks in the new broad peak in case of the low concentration of the graphene oxide in the composite. The increased conjugation comes from the doping of carboxyl acid of graphene oxide to PANI backbone and $\pi-\pi$ stacking of PANI and graphene oxides sheets. The presence of the hydrogen

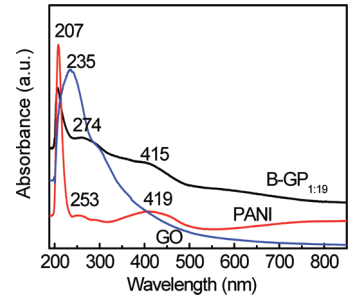

FIGURE 4. UV−vis spectra of PANI, GO (500 mesh), and B-GP$_{1:19}$ in alcohol.

bonds is due to the oxygenous and nitrogenous functional groups in the composite.

The C 1s of C═O peak increased to 288.6 eV, indicating that the COOH groups of graphene oxide were doped into PANI by electrostatic action. Besides, a new peak centered around 286.1 eV attributed to C−N$^{\bullet+}$/C═N$^{\bullet+}$(C−N/C−N) was observed, corresponding to the structure of PANI (38). Remarkably, the $\pi \rightarrow \pi^*$ shakeup satellite peak around 291.5 eV, a characteristic of aromatic or conjugated systems, appeared after reaction, which means the increased conjugation in the composites (39). The XPS peak of O 1s in Figure 3b of graphite oxide are composed of two Gaussian peaks with their binding energy of C−OH (C−O−C) at 533.1 eV and C═O at 532.2 eV, these peaks shift to 533.2 and 531.4 eV in S-GP$_{1:100}$, respectively. The downshift of C═O peak reveals the increased outer electron cloud density of oxygen atoms after doping.

Figure 4 shows UV−vis spectra recorded in alcohol. An absorption peak was observd for graphene oxide at 235 nm. The PANI sample has a sharp intense peak at 207 nm, a weak peak at 253 nm, and a broad peak at 419 nm. The first and second peaks are related to the molecule conjugation. The third absorption peak originates in the charged cationic species, which are known as polarons (36, 40). The last peak shifted to 415 nm in B-GP$_{1:19}$, indicating that the PANI was also protonated in the synthesized composite. Moreover, the two peaks situated at 207 and 274 nm related to the molecule conjugation also can be observed, indicating the $\pi-\pi$ interaction between PANI and graphene oxide of the composite. Therefore, the UV−vis absorption results, together with the Raman spectra and XPS analysis, indicates that PANI chain in the composite is in the doped state. The possible combinding mode of graphene oxide/PANI composite is proposed including: (a) $\pi-\pi$ stacking (b) electrostatic interactions, and (c) hydrogen bonding, as presented in Scheme 1.

Electrochemical Properties. Figure 5 shows representative CVs for S-GP$_{ratio}$ (Figure 5a) and B-GP$_{ratio}$ (Figure 5b) at a scan rate of 10 mV s^{-1} in 1 M H_2SO_4 recorded in the potential range of −0.2 and 1 V, and CVs for S-GP$_{1:23}$ (Figure 5c) and B-GP$_{1:19}$ (Figure 5d) at different scan rates.

Normally, as shown in Figure S2 of the Supporting Information, pure PANI shows two couples of redox peaks. One is due to transition of polyaniline from the semiconducting-state (leucoemeraldine) to the conductive form (emeraldine), the other is due to transition from emeraldine to

Scheme 1. Proposed Possible Combinding Mode of Graphene Oxide/PANI Composite

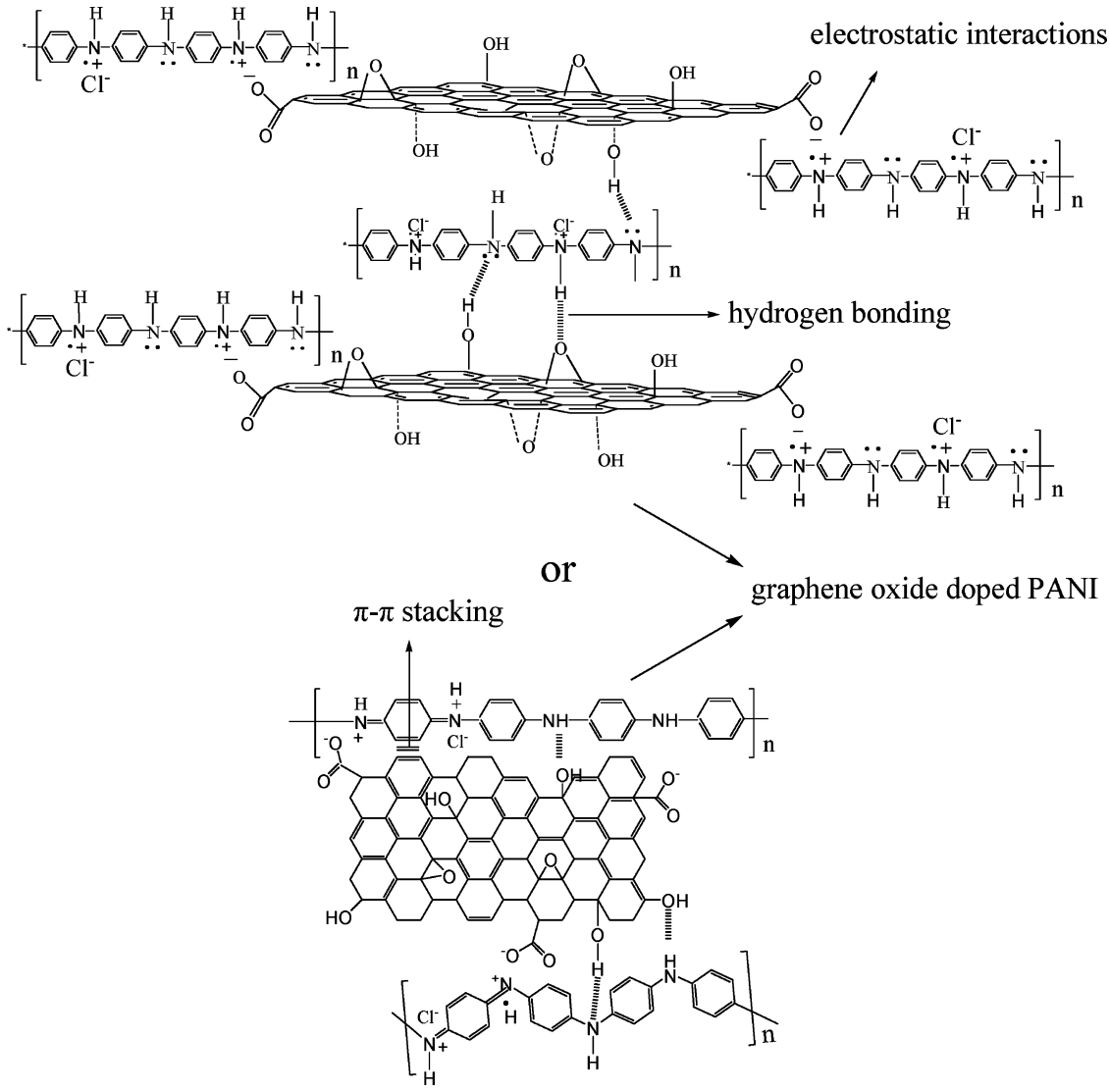

the pernigraniline; the GO electrode also exhibits a pair of peaks that originated from the oxygenous groups on the surface. However, when graphene oxide and PANI are combined into GP_{ratio} composites, their CV curves are different from each component electrode and exhibit the characters of both double layered capacitance and pseudocapacitance (Figure 5a−d). More interestingly, the CV shapes of GP_{ratio} (both $S\text{-}GP_{ratio}$ and $B\text{-}GP_{ratio}$) change with different mass ratios. Because the binder (acetylene black and polytetrafluoroethylene) of each working electrode is inactive and occupies the same amount, the change in CV character is due to the nature of composite materials. The synergetic effect resulting from the interactions of PANI and graphene oxide may affect the shape and potential position of CV curves.

The existence of peak on each CV plot for the samples indicates the existence of the faradic processes. The charge storage in the faradic process is achieved by electron transfer that leads to chemical changes in the electroactive materials according to Faraday's law related to the potential (41). The redox peaks can be ascribed to the changing in PANI structures and the oxygenated groups attached to the surface of the graphene oxide nanostructures. Besides, the surface chemical functional groups significantly influence the interfacial capacitance by introducing pseudocapacitance as depicted in former reports (1, 2, 42−47). Thus, graphene oxide sheets with different amounts in the composites may play an important role in determining the CV shapes.

Compared with the CV of PANI electrode, the capacitance performances of GP_{ratio} were enhanced to different degrees as the mass ratio changes for $S\text{-}GP_{ratio}$ samples with the ratio below 1:15 and for all $B\text{-}GP_{ratio}$ prepared in our experiment. Therefore, the CV behavior actually exhibits the synergetic performance of the two components, PANI and graphene oxide, in the chemically combined composites.

It is notable that the synthesized materials also exhibited excellent electrochemical behavior in a wide range of scan rates (1−100 mV s^{-1}) in H_2SO_4 electrolyte solution. For example, for $S\text{-}GP_{1:23}$ and $B\text{-}GP_{1:19}$, the current density in A g^{-1} of both samples increases with the scan rate and the curve shape is steady, indicating the good electrochemical stability of the electrode material. This is due to the introduc-

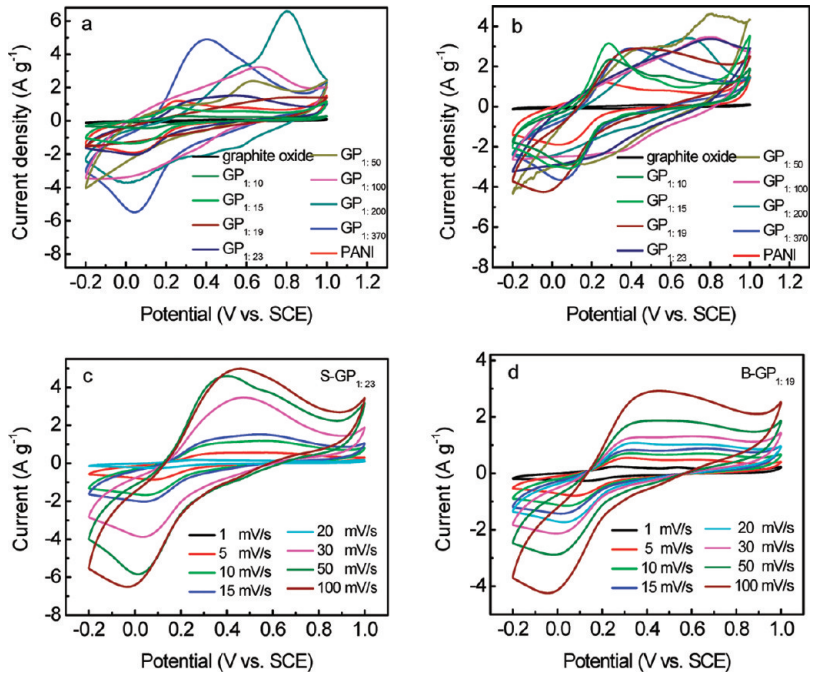

FIGURE 5. CVs of (a) S-GP$_{ratio}$ and (b) B-GP$_{ratio}$ at 10 mV s^{-1} and (c) S-GP$_{1:23}$ and (d) B-GP$_{1:19}$ at different scan rates, in 1 M H_2SO_4 at room temperature.

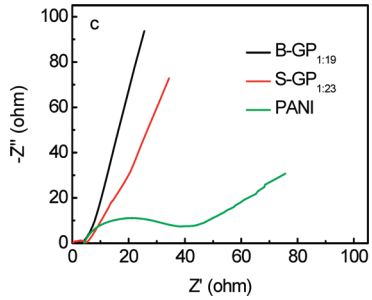

FIGURE 6. Complex plane plots for S-GP$_{1:23}$, B-GP$_{1:19}$, and PANI.

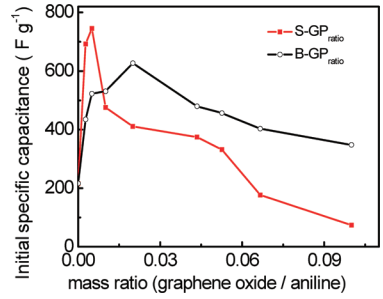

FIGURE 7. Initial specific capacitance of the composites at different mass ratios (graphene oxide/aniline).

tion of graphene oxide with high mechanical property (23) into the composites and the synergetic effect between the two components. The CVs shape of S-GP$_{1:23}$ is a little different from B-GP$_{1:19}$, which is probably related to the different feeding ratios and different faradic charge-transfer reactions arising from the interaction and synergy between individual components.

An electrochemical impedance technique has also been employed in order to understand the difference in the electrochemical behavior between S-GP$_{1:23}$ and B-GP$_{1:19}$ compared with pure PANI with the mass of active material 16.1, 16.5, and 3 mg, respectively. Typical complex plane plots for these electrodes are presented in Figure 6, recorded under the condition: AC voltage amplitude 5 mV, frequency range 1×10^5 to 1×10^{-3} Hz at 0.5 V. At low frequency, the composite electrodes exhibit a more vertical line than pure PANI, showing a better capacitor behavior. At higher frequency, the impedance plot has a relatively small radius, which shows lower resistance. From the point intersecting with the real axis in the range of high frequency, the internal resistance (48) of S-GP$_{1:23}$ and B-GP$_{1:19}$ are much lower than that of PANI. The decreased internal resistance compared with PANI electrode may be due to the doping process and $\pi-\pi$ stacking (40) between graphene oxide and PANI.

The galvanostatic charge−discharge method is a reliable way to characterize the electrochemical capacitance of materials under controlled current conditions (5, 13). Figure 7 represents the changes of initial specific capacitance (C_0) with the mass ratio measured at a constant current density of 200 mA g^{-1} in the potential range of 0.0−0.8 V. The specific capacitance values (5) were calculated from the charging and discharging curves according to $C = I/m(dv/dt)$, where I is the constant discharge current, m is the mass of the active materials within the electrode, and dV/dt can be obtained from the slope of the discharge curve given by the instrument. In genaral, most composites with different ratios for both sizes of graphite exhibit the enhanced specific capacitances compared with pure PANI, indicating the synergistic effect of individual components. S-GP$_{ratio}$ shows the higher C_0 in the lower mass ratio (graphene oxide/aniline) region and lower value in the higher mass ratio region than B-GP$_{ratio}$ as presented in Figure 7. Besides, for GP$_{ratio}$ with the same raw graphite size (both S-GP$_{ratio}$ and B-GP$_{ratio}$), the C_0 goes up sharply to a maximum value and decreases slowly as the content of graphene oxide increases. The maximum

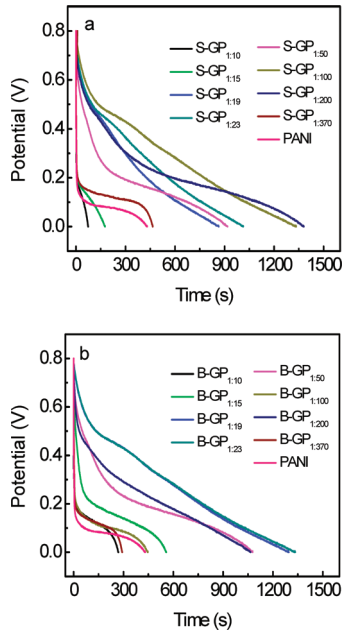

FIGURE 8. Discharge curves of (a) S-GP$_{ratio}$ and (b) B-GP$_{ratio}$ in 1 M H_2SO_4 at 200 mA g^{-1}.

C value for S-GP$_{ratio}$ and B-GP$_{ratio}$ are 746 and 627 F g^{-1}, corresponding to mass ratios of 1:200 and 1:50, respectively. These results are higher than the value obtained by the report (26) synthesized by a electrochemical method. The specific capacitance is higher for the lower mass ratio perhaps because of the lower material resistance. By increasing the mass ratio of graphite oxide as raw material, which in turn became graphene oxide as the experimental process went on, the increased resistance due to the poor conductivity of graphene oxide limits the double layer charging in the electrode depth; only the outer part of the electrode is active, leading to a capacitance loss (49, 50).

Figure 8 shows the discharge curves of S-GP$_{ratio}$ (Figure 8a) and B-GP$_{ratio}$ (Figure 8b) in 1 M H_2SO_4 at a current density of 200 mA g^{-1}, these curves exhibit an evident pseudocapacitance performance as they deviate from perfect linear shape. Generally, the discharge time is enlarged for the majority of GP$_{ratio}$ samples after doping of graphene oxide compared with pure PANI. Moreover, the shape of discharge curves varies for different mass ratios, indicating the difference of charge release process. These changes might be derived from different morphology for different ratios as shown in Figure 1. The mass of GP$_{ratio}$ adopted for charge–discharge measurements and the exact initial specific capacitance in the potential range of 0.0–0.4 V at a current density of 200 mA g^{-1} is presented in Table 1. In spite of the high ohmic drop in galvanostatic profiles for some samples, the results demonstrate that the electrode maintains its high capacitance value. For example, S-GP$_{1:370}$ with a specific capacitance of 693 F g^{-1} is obtained. Moreover, we have examined the performance of samples for which the mass ratio exceeds 1:10 for both S-GP$_{ratio}$ and B-GP$_{ratio}$; the capacitance decreases rapidly (not shown here), even below pure PANI. This is possibly due to the increased amount of graphite oxide with poor conductivity. This result implies that the raw material size and the feeding ratio have a pronounced effect on the electrochemical capacitance behavior.

The cycling performance is also an important aspect to examine the character of electrode material. The cycling life test results (not shown here) indicate that both S-GP$_{ratio}$ and B-G$_{Pratio}$ exhibit better capacitance retention than pure PANI within the mass ratios conducted in our experiments, which is due to the introduction of graphene oxide with good properties (23). Furthermore, S-GP$_{ratio}$ shows better cycling performance than B-GP$_{ratio}$ for the same mass ratio. This is probably because the two components in the composites from smaller graphene oxide sheets can disperse more uniformly and combine more compactly with each other. This enhances the stability of the composites, leading to a better cycling life. Among these ratios, S-GP$_{1:23}$ and B-GP$_{1:19}$ show best cycling character with the capacitance retention of 73% and 64% compared to 20% of PANI after 500 cycles, respectively, which is discussed in detail in the following experiments.

The electrochemical capacitance performances are further investigated for S-GP$_{1:23}$ and B-GP$_{1:19}$ in 1 M H_2SO_4 as shown in Figure 9. The performance between S-GP$_{1:23}$ and B-GP$_{1:19}$ are compared at 1–4 cycles (Figure 9a) and 500–503 cycles (Figure 9b) at a current density of 200 mA g^{-1}. The S-GP$_{1:23}$ and B-GP$_{1:19}$ electrode materials give an initial specific capacitance of 421 and 456 F g^{-1} in the potential range from 0 to 0.4 V, respectively. After 500 cycles, the specific capacitance maintains at 330 and 293 F g^{-1}, which corresponds to 78 and 64% of the initial capacitance, respectively. These values show a pronounced enhancement in capacitance and lifetime compared with pure PANI, the corresponding specific capacitance 216 and 43 F g^{-1} with the capacitance retention 20%. Thus, it is further improved that the graphene-oxide-doped PANI shows a synergistic effect of the two components. The decrease in specific capacitance with cycling is in agreement with other studies on PANI-based redox supercapacitors (51, 52). It is notable that the shape of the curve S-GP$_{1:23}$ and B-GP$_{1:19}$ at cycles 500–503 is a little different than those of cycles 1–4, and the discharge time also decreases, which is probably due to the structure changing with the continuous cycling.

The charge–discharge plots of S-GP$_{1:23}$ and B-GP$_{1:19}$ at different current densities after 500 cycles were given in panels c and d in Figure 9, respectively. At a current density of 400 mA g^{-1}, S-GP$_{1:23}$ and B-GP$_{1:19}$ give a specific capacitance of 305 and 316 F g^{-1} with masses of 8.2 and 13.2 mg, respectively. These values are lower than the specific capacitance obtained at 200 mA g^{-1}, so the specific capacitance strongly depends on current density; this result is consistent with another report (4).

The cycling performances of S-GP$_{1:23}$ and B-GP$_{1:19}$ at 1, 100, 200, 300, 400, and 500 cycles are compared by charge–discharge curves in the voltage of 0.0–0.8 V, as presented in panels e and f in Figure 9. There is no large IR drop even in the last cycle for both samples; as the cycles increased to cycle 500, the capacitance experiences a

Table 1. Weight and Initial Specific Capacitance (calculated in the potential range of 0−0.4 V) of S-GP_{ratio} and B-GP_{ratio} Used for Charge-Discharge Measurements at 200 mA g^{-1}

	GP_{ratio}	$GP_{1:10}$	$GP_{1:15}$	$GP_{1:19}$	$GP_{1:23}$	$GP_{1:50}$	$GP_{1:100}$	$GP_{1:200}$	$GP_{1:370}$	PANI
mass (mg)	S-GP_{ratio}	11.8	9.8	11.4	18	8.2	14	5.3	5	2
	B-GP_{ratio}	2.4	2.9	16.1	13.9	4.1	2.8	7.6	4.6	2
C_0 (F g^{-1})	S-GP_{ratio}	74	177	332	375	411	476	746	693	216
	B-GP_{ratio}	348	429	456	479	627	530	520	435	216

smooth fading and the shape of curves keeps a little difference with the first cycling and almost the same as cycle 100. Though the initial specific capacitance of S-$GP_{1:23}$ is lower than that of B-$GP_{1:19}$, the cycling performance of S-$GP_{1:23}$, synthesized from smaller graphene oxide sheets, is better than that of B-$GP_{1:19}$. The charge−discharge characterization demonstrates that the graphene-oxide-doped PANI owns not only a high initial specific capacitance but also an enhanced cycling life when a proper feeding ratio is adopted. A recent report given by Wu et al. (53) revealed that the number of layers of graphene oxide obtained by heating was different for the two raw graphite sizes. However, according to the XRD analysis (shown in Figure S2 in the Supporting Information) in our conditions, graphene oxide is mainly a single layer due to the missing reflection peaks of S- and B- graphite oxide at ∼10° in composites S-$GP_{1:23}$ and B-$GP_{1:19}$. The highly dispersed graphene oxide sheets in the composite may play an important role in the improved cycling life.

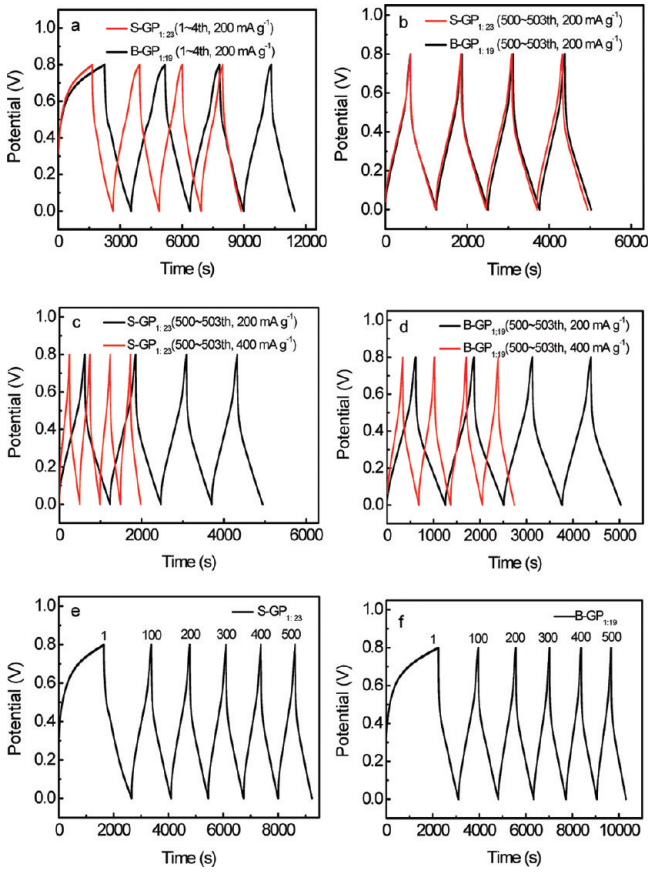

FIGURE 9. Galvanostatic charge−discharge curves in 1 M H_2SO_4 between 0 V and 0.8 V. S-$GP_{1:23}$, B-$GP_{1:19}$ (a) at initial 4 cycles and (b) after 500 cycles at a current density of 200 mA g^{-1}. (c) S-$GP_{1:23}$ and (d) B-$GP_{1:19}$ at different current densities of 200 mA g^{-1} and 400 mA g^{-1}, respectively. (e) S-$GP_{1:23}$ and (f) B-$GP_{1:19}$ at 1, 100, 200, 300, 400, 500 cycles at a current density of 200 mA g^{-1}.

CONCLUSIONS

This paper presents high performances of graphene-oxide-doped PANI nanocomposites synthesized by soft chemical method for supercapacitors. The nanocomposites exhibit excellent capacitance as high as 2 times that with pure PANI below the mass ratio 1:50 for S-GP and 1:15 for B-GP. The retention on cycling can be enhanced greatly by adjusting the feeding ratio of materials. The raw material sizes and the ratio of graphene oxide have a pronounced effect on the electrochemical performance of the nanocomposites. Such nanocomposites can be expected to show maximum capacitance and cycling life if further optimization of the experimental condition is done. The product shows good application potential in supercapacitors or other power source system.

Acknowledgment. This work was supported by Natural Science Foundation of China and China Academy of Engineering Physics (10776014), Science and Technology Surporting item of Jiangsu Province, China (BE2009159). SRF for ROCS, State Education Ministry and Ministry of Personnel of the PRC (2006), and Excellent Plan Foundation of NUST (2008).

Supporting Information Available: Experimental procedures and X-ray diffraction of graphite oxide and its composite (PDF). This material is available free of charge via the Internet at http://pubs.acs.org.

REFERENCES AND NOTES

(1) Kodama, M.; Yamashita, J.; Soneda, Y.; Hatori, H.; Kamegawa, K. *Carbon* **2007**, *45*, 1105–1136.
(2) Hulicova, D.; Kodama, M.; Hatori, H. *Chem. Mater.* **2006**, *18*, 2318–2326.
(3) Patrice, S.; Gogotsi, Y. *Nat. Mater.* **2008**, *7*, 845–854.
(4) Gupta, V.; Miura, N. *Electrochim. Acta* **2006**, *52*, 1721–1726.
(5) Cao, Y.; Mallouk, T. E. *Chem. Mater.* **2008**, *20*, 5260–5265.
(6) Snook, G. A.; Chen, G. Z. *J. Electroanal. Chem.* **2008**, *612*, 140–146.
(7) Ferraris, J. P.; Eissa, M. M.; Brotherston, I. D.; Loveday, D. C. *Chem. Mater.* **1998**, *10*, 3528–3535.
(8) Palaniappan, S.; Devi, S. L. *J. Appl. Polym. Sci.* **2008**, *107*, 1887–1892.
(9) Prasad, K. R.; Munichandraiah, N. *J. Power Sources* **2002**, *112*, 443–451.
(10) Jang, J.; Bae, J.; Choi, M.; Yoon, S. H. *Carbon* **2005**, *43*, 2730–2736.
(11) Wang, Y. G.; Li, H. Q.; Xia, Y. Y. *Adv. Mater.* **2006**, *18*, 2619–2623.
(12) Fan, L. Z.; Hu, Y. S.; Maier, J.; Adelhelm, P.; Smarsly, B.; Antonietti, M. *Adv. Funct. Mater.* **2007**, *17*, 3083–3087.
(13) Zhang, X.; Ji, L.; Zhang, S.; Yang, W. *J. Power Sources* **2007**, *173*, 1017–1023.
(14) Stoller, M. D.; Park, S. J.; Zhu, Y. W.; An, J.; Ruoff, R. S. *Nano Lett.* **2008**, *8*, 3498–3502.
(15) Stankovich, S.; Dikin, D. A.; Dommett, G. H. B.; Kohlhaas, K. M.; Zimney, E. J.; Stach, E. A.; Piner, R. D.; Nguyen, S. B. T.; Ruoff, R. S. *Nature* **2006**, *442*, 282–286.

(16) Shen, J. F.; Hu, Y. Z.; Li, C.; Qin, C.; Ye, M. X. *Small* **2009**, *5*, 82–85.
(17) Raghu, A. V.; Lee, Y. R.; Jeong, H. M.; Shin, C. M. *Macromol. Chem. Phys.* **2008**, *209*, 2487–2493.
(18) Shin, H. J.; Kim, J.; Benayad, A.; Yoon, S. M.; Park, H. K.; Jung, I. S.; Jin, M. H.; Jeong, H. K.; Kim, J. M.; Choi, J. Y.; Lee, Y. H. *Adv. Funct. Mater.* **2009**, *19*, 1987–1992.
(19) Sundaram, R. S.; Gómez-Navarro, C.; Balasubramanian, K.; Burghard, M.; Kern, K. *Adv. Mater.* **2008**, *20*, 3050–3053.
(20) Ang, P. K.; Chen, W.; Wee, A. T. S.; Loh, K. P. *J. Am. Chem. Soc.* **2008**, *130*, 14392–14393.
(21) Jung, I.; Dikin, D. A.; Piner, R. D.; Ruoff, R. S. *Nano Lett.* **2008**, *8*, 4283–4287.
(22) Warner, J. H.; Schäffel, F.; Rümmeli, M. H.; Büchner, B. *Chem. Mater.* **2009**, *21*, 2418–2421.
(23) Dikin, D. A.; Stankovich, S.; Zimney, E. J.; Piner, R. D.; Dommett, G. H. B.; Evmenenko, G.; Nguyen, S. T.; Ruoff, R. S. *Nature* **2007**, *448*, 457–460.
(24) Si, Y.; Samulski, E. T. *Nano Lett.* **2008**, *8*, 1679–1682.
(25) Wang, Y.; Shi, Z. Q.; Huang, Y.; Ma, Y. F.; Wang, C. Y.; Chen, M. M.; Chen, Y. S. *J. Phys. Chem. C* **2009**, *113*, 13103–13107.
(26) Wang, D. W.; Li, F.; Zhao, J. P.; Ren, W. C.; Chen, Z. J.; Tan, J.; Wu, Z. S.; Gentle, I.; Lu, G. Q.; Cheng, H. M. *ACS Nano* **2009**, *3*, 1745–1752.
(27) Wei, T.; Luo, G. L.; Fan, Z. J.; Zheng, C.; Yan, J.; Yao, C. Z.; Li, W. F.; Zhang, C. *Carbon* **2009**, *47*, 2290–2299.
(28) Wang, H. L.; Hao, Q. L.; Yang, X. J.; Lu, L. D.; Wang, X. *Electrochem. Commun.* **2009**, *11*, 1158–1161.
(29) Kovtyukhova, N. I.; Ollivier, P. J.; Martin, B. R.; Mallouk, T. E.; Chizhik, S. A.; Buzaneva, E. V.; Gorchinskiy, A. D. *Chem. Mater.* **1999**, *11*, 771–778.
(30) Li, D.; Mẗller, M. B.; Gilje, S.; Kaner, R. B.; Wallace, G. G. *Nature nano.* **2008**, *3*, 101–105.
(31) Sun, Z. C.; Geng, Y. H.; Li, J.; Jing, X. B.; Wang, F. S. *Synth. Met.* **1997**, *84*, 99–100.
(32) Kang, H.; Kulkarni, A.; Stankovich, S.; Ruoff, R. S; Baik, S. *Carbon* **2009**, *47*, 1520–1525.
(33) Kudin, K. N.; Ozbas, B.; Schniepp, H. C.; Prudhomme, R. K.; Aksay, I. A.; Car, R. *Nano Lett.* **2008**, *8*, 36–41.
(34) Ganesan, R.; Shanmugam, S.; Gedanken, A. *Synth. Met.* **2008**, *158*, 848–853.
(35) Markovic, M. G.; Matisons, J. G.; Cervini, R.; Simon, G. P.; Fredericks, P. M. *Chem. Mater.* **2006**, *18*, 6258.
(36) Wei, Z.; Wan, M.; Lin, Tong.; Dai, L. *Adv. Mater.* **2003**, *15*, 136–139.
(37) Park, S.; An, J.; Piner, R. D.; Jung, I.; Yang, D.; Velamakanni, A.; Nguyen, S. T.; Ruoff, R. S. *Chem. Mater.* **2008**, *20*, 6592–6594.
(38) Golczak, S.; Kanciurzewska, Anna.; Fahlman, M.; Langer, K.; Langer, J. J. *Solid State Ionics* **2008**, *179*, 2234–2239.
(39) Fan, X.; Peng, W.; Li, Yang.; Li, X.; Wang, S.; Zhang, G.; Zhang, F. *Adv. Mater.* **2008**, *20*, 1–4.
(40) Lin, Y. W.; Wu, T. M. *Compos. Sci. Technol.* **2009**, *69*, 2559–2565.
(41) Conway, B. E. *Electrochemical Supercapacitors: Scientific Fundamentals and Technological Applications*; Kluwer Academic/Plenum: New York, 1999.
(42) Hulicova, D.; Yamashita, J.; Soneda, Y.; Hatori, H.; Kodama, M. *Chem. Mater.* **2005**, *17*, 1241–1247.
(43) Ania, C. O.; Khomenko, V.; Raymundo-Pinero, E.; Parra, J. B.; Beguin, F. *Adv. Funct. Mater.* **2007**, *17*, 1828–1836.
(44) Kim, Y. J.; Abe, Y.; Yanaglura, T.; Park, K. C.; Shimizu, M.; Iwazaki, T.; Nakagawa, S.; Endo, M.; Dresselhaus, M. S. *Carbon* **2007**, *45*, 2116–2115.
(45) Li, W. R.; Chen, D. H.; Li, Z.; Shi, Y. F.; Wan, Y.; Huang, J. J.; Yang, J. J.; Zhao, D. Y.; Jiang, Z. Y. *Electrochem. Commun.* **2007**, *9*, 569–573.
(46) Frackowiak, E.; Lota, G.; Machnikowski, J.; Vix-Guterl, C.; Beguin, F. *Electrochim. Acta* **2006**, *51*, 2209–2214.
(47) Raymundo-Pinero, E.; Leroux, F.; Beguin, F. *Adv. Mater.* **2006**, *18*, 1877–1882.
(48) Dandekar, M. S.; Arabale, G.; Vijayamohanan, K. *J. Power Sources* **2005**, *141*, 198–203.
(49) Portet, C.; Taberna, P. L.; Simon, P.; Flahaut, E.; Robert, C. L. *Electrochim. Acta* **2005**, *50*, 4174–4184.
(50) Pell, W. G.; Conway, B. E.; Marincic, N. *J. Electroanal. Chem.* **2000**, *491*, 9–21.
(51) Sivakkumar, S. R.; Kim, W. J.; Choi, J.; MacFarlane, D. R.; Forsyth, M.; Kim, D. *J. Power Sources* **2007**, *171*, 1062–1068.
(52) Park, J. H.; Park, O. O.; El, H. *J. Power Sources* **2002**, *111*, 185–190.
(53) Wu, Z. S.; Ren, W.; Gao, L.; Liu, B.; Jiang, C.; Cheng, H. M. *Carbon* **2009**, *47*, 493–499.

AM900815K